Rubredoxin protein scaffolds sourced from diverse environmental niches as an artificial hydrogenase platform

Ashlee E. Wertz[a], *Pathorn Teptarakulkarn*[a], *Riley E. Stein*[a], *Peter J. Moore*[a], *Hannah S. Shafaat*[a]*

[a]Department of Chemistry and Biochemistry, The Ohio State University, 100 W 18th Avenue, Columbus, Ohio 43210, United States

hydrogen production, artificial metalloenzyme, protein film electrochemistry, nickel, psychrophilic organisms

ABSTRACT

Nickel-substituted rubredoxin (NiRd) from *Desulfovibrio desulfuricans* has previously been shown to act as both a structural and functional mimic of the [NiFe] hydrogenase. However, improvements both in turnover frequency (TOF) and overpotential are needed to rival the native [NiFe] hydrogenase enzymes. Characterization of a library of NiRd mutants with variations in the secondary coordination sphere suggested protein dynamics played a substantial role in modulating activity. In this work, rubredoxin scaffolds were selected from diverse organisms to study the effects of distal sequence variation on catalytic activity. It was found that though electrochemical

catalytic activity was only slightly impacted across the series, the Rd sequence from a psychrophilic organism exhibited substantially higher levels of solution-phase hydrogen production. Additionally, Eyring analyses suggest that catalytic activation properties relate to the growth temperature of the parent organism, implying that the general correlation between parent organism environment and catalytic activity often seen in naturally occurring enzymes may also be observed in artificial enzymes. Selecting protein scaffolds from hosts that inhabit diverse environments, particularly low temperature environments, represents an alternative approach for engineering artificial metalloenzymes.

INTRODUCTION

Hydrogen gas is a promising alternative to traditional carbon-based fuels. However, the most widely used method for generating hydrogen gas relies on the steam reforming of methane,[1,2] which still contributes to rising CO_2 levels and thus is not sustainable. In nature, metalloenzymes known as hydrogenases have evolved to produce hydrogen directly from water, under mild conditions, using only first-row transition metals such as iron and nickel.[3–5] The [NiFe] hydrogenase contains a heterobimetallic nickel-iron active site, with the Ni center identified as the redox-active metal responsible for reversibly reducing protons and electrons to hydrogen gas.[6,7] Despite the effectiveness of this enzyme *in vivo*, the large scale application of hydrogenases remains intractable for several reasons, including high sensitivity to oxygen and difficulties in heterologous expression.[8,9]

Previous work from our lab and others has shown that rubredoxin (Rd), a small electron transfer (ET) protein that natively binds Fe, can be substituted with a variety of metals, including Ni.[10–12] Nickel-substituted rubredoxin (NiRd) has a tetrathiolate active site that reproduces the primary

coordination sphere found in the [NiFe] hydrogenase. We have demonstrated that NiRd is capable of both electrochemical and solution-phase hydrogen production, with additional advantages relative to the native enzyme.[13] First, this protein is small but well-folded, which enables heterologous expression in *E. coli* and provides stability towards changes in pH and temperature.[14] Second, NiRd activity is insensitive to oxygen exposure.[15] Third, the primary and secondary coordination spheres around the catalytic Ni center are easily modulated to tune reactivity.[16] These advantages make NiRd an ideal platform for both producing hydrogen gas and studying the effects that subtle variations in protein sequence have on activity.

Past studies from our group have focused on a Ni-substituted Rd originating from the mesophilic, sulfate-reducing bacterium *Desulfovibrio desulfuricans* (*Dd*). While this artificial enzyme is active, improvements both in turnover frequency (TOF) and overpotential are needed to rival the native [NiFe] hydrogenases.[15,17] *Dd* NiRd exhibits a moderate overpotential of approximately 560 mV and evolves H_2 with turnover frequencies (TOFs) around 30 s^{-1}, [15] while [NiFe] hydrogenases have been shown to operate at the thermodynamic potential and reach TOFs that are approximately an order of magnitude higher.[18] Recent efforts to understand how secondary sphere interactions modulate catalysis in a rationally designed *Dd* NiRd mutant library provided valuable insight into how hydrogen bonding and solvent accessibility may influence activity. Specifically, though acidic functional groups were inserted to install proton-transfer networks, local flexibility and protein dynamics were instead suggested to be the dominant cause in increasing catalytic rates, highlighting the challenges of using targeted design in enzyme engineering.[16] As individual mutations were not found to be reliable predictors of activity, other approaches can complement rationally designed libraries to develop increasingly productive catalysts.

Rubredoxin proteins are found in a wide variety of bacteria and archaea with highly conserved sequences and strictly conserved primary sphere residues.[19,20] Motivated by prior findings that suggested transient conformational changes could drive enhanced catalysis,[16] we sought to explore whether catalytic activity might be impacted by remote variations in sequence that change with the optimal growth temperature of the parent organism. Rubredoxin sequences from psychrophilic, mesophilic, and hyperthermophilic organisms were identified and substituted with nickel. Catalytic characterization of each variant revealed that while electrochemical catalytic activity was only slightly impacted by the sequence variation, nickel-substituted Rd from a psychrophilic organism exhibited substantially higher levels of solution-phase hydrogen production. Paramagnetic NMR lineshape analysis indicates distinct dynamical behavior of this Rd, suggesting a potential link between protein structural variability and catalytic properties. Exploring the impact of changes in non-conserved residues as organisms adapt to their growth environment represents a new avenue for artificial catalyst design and optimization.

MATERIALS AND METHODS

Bioinformatics Analysis

A sequence similarity network (SSN) was generated for InterPro Entry IPR024934 (Rubredoxin-like domain) using the web resource tool developed by the Enzyme Function Initiative (EFI).[21] Option B was used which generates a SSN for a protein family. The protein sequence length was constrained from a minimum length of 30 to a maximum length of 100 in order to exclude small fragments as well as sequences that would be too long to easily heterologously express. An alignment score of 23 was used. Each cluster was assigned a unique color and visualized in Cytoscape.[22] Sequence alignment was carried out through the Expresso alignment tool within T

Coffee and color-coded using the ENDscript server.[23] A sequence logo was generated for the rubredoxin domain (IPR024935) using the Clustal Omega Multiple Sequence Alignment tool[24] to position the sequences and WebLogo[25] to generate the sequence logos.

Homology Modeling

Protein structures were modeled using the AlphaFold Colab notebook, a version of AlphaFold v2.1.0[26,27] (Figure S1).

Protein Expression and Purification

Rubredoxin protein sequences were ordered through Life Technologies with pET303_CT-His as the expression vector (Figure S2). The Rd sequences ordered were from *Acetobacterium woodii* (*Aw;* UniProtKB H6LCE6), *Psychrobacter sp. P11G5* (*Pg;* UniProtKB A0A127GYZ6), *Methanocaldococcus jannaschii* (*Mj;* UniProtKB Q58150), and *Pyrococcus furiosus* (*Pf*; UniProtKB P24297), and compared to that of *Desulfovibrio desulfuricans* ATCC 27774 (*Dd*; UniProtKB P04170). The proteins were truncated with three sequential TAA stop codons prior to the commercial His tag and expressed tag-less (Figure S3). The plasmids were transformed into DH5α competent *E. coli* cells and isolated using a QIAprep Spin Miniprep Kit (QIAGEN). Prior to experimentation, all variants were sequenced to ensure that no unwanted mutations were present. After sequencing, the vector was transformed into competent BL-21 *E. coli* cells, and proteins were expressed and purified as previously described. Ni, Fe, or Zn was incorporated into each of the variants using the previously described TCA preparation,[13] and protein purity was confirmed by gel electrophoresis (Figure S4).

Electrochemistry

All electrochemistry experiments were carried out in a nitrogen glovebox. Protein samples were electrostatically adsorbed to the electrode by aliquoting 10 µL of a 1:1 Fe^{II}Rd:Ni^{II}Rd 250 µM total protein solution onto the pyrolytic graphite (PG) electrode, allowing the solution to sit for 30 seconds, and then removing any excess liquid. Fe^{II}Rd samples were prepared as previously described.[28] All protein solutions were adsorbed at pH 4.0 except for *Pg* Rd, which was adsorbed at pH 4.5 because of stability issues at lower pH values. Quantitative protein film electrochemistry (qPFE) was used to determine the turnover frequency (TOF; Equation 1),[15] where Γ_{NiRd} is the electroactive coverage of NiRd, i is the current measured at 100 mV more negative than the onset of catalysis, n is the number of electrons transferred in the reaction and F is Faraday's constant.

$$TOF = \frac{i}{\Gamma_{NiRd} nF} \quad (1)$$

The onset potential was obtained as described previously.[15] For covalently attached experiments, the protein was attached using 1-ethyl-3-(3-dimethylaminopropyl) carbodiimide hydrochloride (EDC) (Sigma- Aldrich) and N-hydroxysuccinimide (NHS) (Sigma-Aldrich) as coupling reagents.[28] Stock solutions were made of 1.8 M EDC and 1.5 M NHS. An 80 µL solution was prepared containing final concentrations of 144 mM EDC, 72 mM NHS and a 1:1 mixture of Fe^{III}Rd:Ni^{II}Rd to a final concentration of 200 µM total protein. It has been previously shown that the FeRd oxidation state does not impact the amount or ratio of protein coupled to the electrode in covalent attachment studies.[28] The Rd variants were all coupled to freshly polished PG electrodes in this solution for 1.5 hours at room temperature. The stability of each variant with the coupling reagents was determined by monitoring the decrease in the ligand-to-metal charge transfer (LMCT) band at ~455 nm for NiRd or ~490 nm for FeRd over the course of 90 minutes (Figure

S5) to assess degradation. A rotating disk electrode was not required for electrochemical studies as NiRd catalysis is unidirectional for proton reduction; therefore, activity is not inhibited by the formed H_2.

A Laviron-type analysis was performed on each covalently attached FeRd variant.[29] As the scan rates were increased, the peak separation for the Fe^{III}/Fe^{II} one-electron redox process also increased. The anodic and cathodic FeRd peak positions were determined using the qSOAS program.[30] The peak positions were fit using Butler-Volmer electron transfer (ET) theory[31] in the JellyFit program to determine interfacial ET rates (Figure S6).[32] A Laviron-type analysis was also performed with the Ni-substituted variants, examining the position of the anodic feature that appears on the return anodic sweep at fast scan rates to estimate the NiRd interfacial ET rate (Figure S7). We note that this analysis was only successful for the electrostatically adsorbed variants.

The solvent isotope effect of each covalently attached NiRd variant was determined by obtaining the currents 100 mV more negative than the onset of catalysis in protiated and deuterated 150 mM sodium acetate buffer, pL 4.5. The ratio of the two currents ($i_{X_{D_2O=1}}/i_{X_{D_2O=0}}$) gives the reported kinetic isotope effect (KIE). Similarly, a proton inventory analysis was performed by measuring the current with varying amounts of deuterated buffer (Figure S8).

Variable temperature experiments were performed on the covalently attached NiRd variants. The current at each temperature is reported at a potential value that is 100 mV more negative than the onset of catalysis at the given temperature, normalized to that at 292 K (Figure S9).

Electrochemical Simulations

Electrochemical data was simulated using in-house Matlab scripts based on previously developed Mathematica scripts.[15] Dispersion was accounted for by modeling the distance from each lysine residue and/or the N-terminus to the active site and assuming the protein could attach at any distance between these values with equal probability. Distances were determined for *Dd* Rd and *Pf* Rd using the published crystal structures[16,33] and estimated for the remaining variants using the Alpha Fold structures, as described above (Figure S10).[26,27] A CECEC mechanism, where "C" refers to a chemical process while "E" refers to an electron transfer step, was used to simulate the electrochemical behavior of all variants due to the overall similarity in the catalytic waveshape and apparent properties to the previously studied voltammograms of *Dd* NiRd. The differential rate laws were written into Matlab and the ordinary differential equation solver ode23tb was used for integration. Simulated TOFs and onset potentials were heuristically modeled to the experimental data to estimate the rate constant k_1 and the pK_a value of the intramolecular proton donor. A sample Matlab script is included in the Supporting Information (Appendix 1).

Absorption Spectroscopy

UV-visible spectra were measured using a Shimadzu UV-2600 spectrophotometer. Extinction coefficients were experimentally determined through use of a bicinchoninic acid protein assay kit (Sigma-Aldrich) (Figure S11).

Gas Chromatography

All gas chromatography (GC) assays were carried out using a Shimadzu GC-2014 fuel cell analyzer coupled to a packed Supelco 60/80 5-angstrom molecular sieve column with a Shimadzu

TCD-2014 thermal conductivity detector. Samples were prepared in a 20 mL GC vial under nitrogen (<10 ppm O_2, MBRAUN) and contained 10 μM NiRd or FeRd, 10 μM $[Ru(bpy)_3]^{2+}$ and 100 mM ascorbate in 1 M phosphate buffer, pH 6.5, to a final volume of 3 mL. Photodriven assays were carried out by placing the solution in a custom-built water-jacketed glass cell with a Rebel ES LED light (447 nm) placed under the vial and a string of blue lights (450 nm) placed around the cell. Samples were either cooled to 4°C (IKA RC 2) or warmed to 37°C (Lauda Brinkmann RM6) using a recirculating pump. 250 μL aliquots were taken from the headspace above the solution using a gas-tight Hamilton syringe. Hydrogen gas was quantified by comparing to a gas standard curve run on the same analytical method (Scotty Analyzed Gases, A0908910).

Fluorescence and Time-Correlated Single-Photon Counting Experiments

Emission measurements were carried out on a Cary Eclipse fluorometer with excitation at 285 nm and emission monitored from 300-440 nm. The Zn-substituted Rd variants were studied instead of the NiRd variants because the S =1 Ni^{II} center can quench fluorescence through Dexter and Förster mechanisms. The bimolecular quenching rate constant was determined at 5 °C, 25 °C, and 37 °C for each of the variants using varying concentrations of acrylamide as the quencher. Time-resolved single-photon counting emission measurements were carried out using a Fluoro-Max-4 spectrofluorometer with excitation at 285 nm.

NMR Spectroscopy

1D ^1H spectra of the protein region (-100 – 100 ppm) were collected at room temperature on Bruker Avance Neo (400 MHz) spectrometer equipped with PABBO400S1 BBF-H-D-05 Z probe using a standard excitation sculpting pulse sequence (*zgespg*) from the Bruker pulse library for water suppression and a Bruker Ascend (850 MHz) spectrometer equipped with triple resonance inverse

TCI cryoprobe (HCN) with z-gradients using the *zgesgppe* pulse sequence from the Bruker pulse library for water suppression. 1D ^{1}H spectra of the paramagnetically shifted peaks (100 – 450 ppm) were collected at room temperature on a Bruker Fourier 80 (80 MHz) spectrometer. Variable temperature experiments were collected at 277 K, 298 K, and 310 K on the Bruker Avance Neo (400 MHz) spectrometer.

All NMR samples were prepared to a final protein concentration of 100 – 220 μM in 10 mM PO_4, pH 8.0, containing 10% D_2O. The spectra were indirectly referenced to DSS through small amounts of excess remaining Tris buffer (used in the stock protein solutions) (δ_{DSS} = 0 ppm, δ_{Tris} = 3.655 ppm (277 K), 3.651 ppm (298 K), 3.643 ppm (310 K)).

RESULTS

Bioinformatics Analyses Guide Identification of Novel Rd Variants for Characterization

A sequence conservation logo of the rubredoxin domain (IPR024935) indicates that this primary sequence is highly conserved (**Figure 1A**). Thus, in order to find diverse sequences to study, a sequence similarity network (SSN) was generated to visualize distinct clusters of ~40,000 known Rd and Rd-like proteins found across sequenced genomes (Figure S12). The *Dd* Rd appears to be unique from other Rds, as it is not connected to other sequences at the indicated alignment score (Figure S13). Four other Rds from parent organisms that survive under diverse environmental conditions were chosen for study. These sequences were selected from across the SSN rather than from the same cluster to ensure diversity. Of the chosen Rd sequences, one derives from a mesophilic acetogenic bacterium, *Acetobacterium woodii* (*Aw*), one sequence was chosen from the psychrophilic bacterium *Psychrobacter sp. P11G5* (*Pg*),[34] and two were chosen from hyperthermophilic archaea (*Methanocaldococcus jannaschii* (*Mj*) and *Pyrococcus furiosus* (*Pf*)).

It should be noted that throughout this work, the term "variant" is used to describe homologous proteins from different organisms, while "mutant" is used to describe a protein in which select amino acids differ from the parent wild-type sequence.

Sequence alignment of the five genes reveals that 71% of residues are strictly or highly conserved (**Figure 1B**), including a defined hydrophobic region.[35] The *Dd* Rd is the smallest Rd, having only

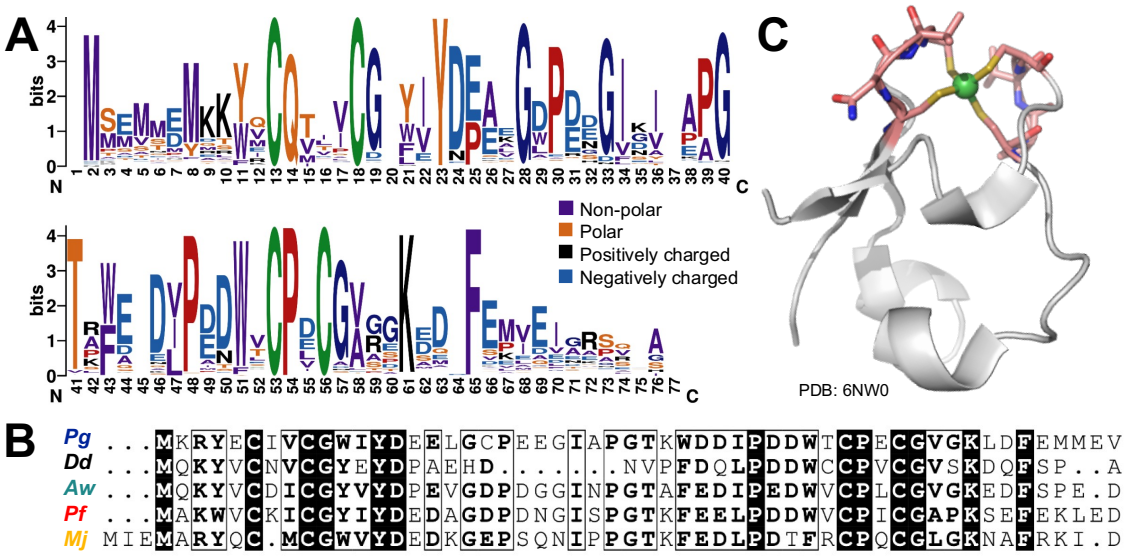

Figure 1. (**A**) Sequence conservation logo for the rubredoxin domain (IPR024935). (**B**) Sequence alignment of selected variants, with strictly and highly conserved residues highlighted in gray and black, respectively. (**C**) X-ray crystal structure of *Dd* NiRd.[16] Active site loops shown with secondary sphere residues highlighted.

45 amino acids and lacking an extended hydrophobic core, while the *Mj* Rd is the largest, with 55 residues. The N-terminal canonical CXXC binding loop in *Mj* Rd is replaced with the CMC sequence, reflecting the only variation in the metal-binding loops across the sequences analyzed. The second sphere residues between the two binding sites in the CXXC loops differ across the variants, as do the degrees of hydrophobicity within the core.

Insertion of nickel into the metal binding site was carried out using a standard trichloroacetic acid precipitation protocol and validated using inductively coupled plasma mass spectrometry (Table ST1) and optical spectroscopy (Figure S14). All Ni-substituted variants show similar spectral features, with sulfur-to-nickel LMCT bands around 370 and 455 nm that exhibit extinction coefficients similar to that of *Dd* NiRd. Interestingly, slight shifts in the position and intensities of the d-d transitions are observed in the low energy region,[36] particularly for the *Mj* and *Pf* Rds, reminiscent of the changes seen in a library of *Dd* Rds with mutations in the secondary coordination sphere.[16]

All NiRd Variants are Active for Electrochemical Proton Reduction

Protein film electrochemistry, a workhorse technique for the study of redox enzymes, has proven quite valuable for characterizing the activity of *Dd* NiRd.[15] Cyclic voltammograms (CVs) of *Dd* FeRd show a reversible one-electron redox couple at ~10 mV vs NHE, while CVs of *Dd* NiRd show large catalytic currents that have been attributed to electrochemical proton reduction (Figure S15).[13] In this work, two different approaches are used for generating Rd protein films, including electrostatic adsorption to the negatively charged surface of a PG electrode and covalent attachment to the carboxylate functional groups using peptide bond coupling chemistry.[28] Both methods were successful for attaching the Rd variants to a PG electrode surface (**Figure 2**).

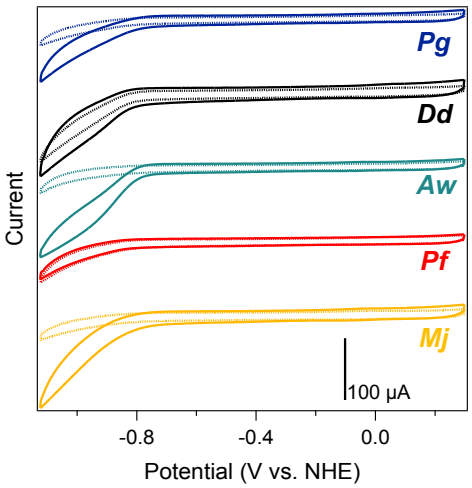

Figure 2. Cyclic voltammograms comparing electrostatically adsorbed (solid lines) and covalently attached (dotted lines) Rd variants in 150 mM acetate buffer, pH 4.5 (ν = 100 mV/s). A 1:1 mixture of FeRd:NiRd was used to determine TOF, as described above.

Using the qPFE analysis methodology presented in Ref. 15, metrics for the electrochemical activity were determined for each of the variants (**Table 1**). The *Dd* and *Aw* variants were the most active when electrostatically adsorbed, with TOF values of 31 ± 8 s^{-1} and 31 ± 3 s^{-1}, respectively. The *Pf*, *Mj* and *Pg* variants were also active for hydrogen production when electrostatically adsorbed, but with smaller TOF values of 20 ± 1 s^{-1} , 13 ± 2 s^{-1} and 9 ± 1 s^{-1} , respectively. A Laviron-type analysis suggests that the slightly higher levels of activity for *Dd* and *Aw* NiRd may derive from increased interfacial electron transfer (ET) rates (**Table 1**, Figure S7). When developing methods for attachment of Rd to an electrode surface, we had previously noted that the *Dd* NiRd qPFE TOFs decreased significantly upon covalent attachment relative to simple electrostatic adsorption. This had been attributed to reduced dynamics,[28] analogous to the decreased ET rates seen in synthetic compounds that had been tethered to surfaces and ET proteins that had been subjected to high viscosity environments.[37–40] A similar observation is made for the variants, with TOFs decreasing by up to an order of magnitude for the *Dd*, *Aw*, *Pf*, and *Mj* NiRds (**Table 1**). An exception was found in the *Pg* variant, for which the TOFs didn't change. Beyond TOFs, no systematic trends emerged from comparing the observed overpotentials, $Fe^{III/II}$Rd reduction potentials, or interfacial FeRd ET rates across the variants (Figure S16).

Table 1. Electrochemical properties of NiRd and FeRd variants.

	Electrostatic Adsorption				**Covalent Attachment**				
	$E^{\circ\prime}$ ($Fe^{III/II}$Rd) (mV vs. NHE)	TOF (s^{-1})	η @ pH 4.5 (mV vs. NHE)	Est. $k_{ET, NiRd}$ (s^{-1})	$E^{\circ\prime}$ ($Fe^{III/II}$Rd) (mV vs. NHE)	$k_{ET, FeRd}$ (s^{-1})	TOF (s^{-1})	η @ pH 4.5 (mV vs. NHE)	KIE (pH 4.5)
Pg	-82 ± 5	9 ± 1	546 ± 10	30	4 ± 10	1320 ± 500	8 ± 2	555 ± 3	1.64 ± 0.12
Dd	4 ± 9	31 ± 8	562 ± 6	120	34 ± 7	680 ± 90	10 ± 5	562 ± 1	1.76 ± 0.08
Aw	-120 ± 20	31 ± 3	528 ± 1	130	-92 ± 2	1060 ± 10	3 ± 1	560 ± 5	1.69 ± 0.14
Pf	4 ± 2	20 ± 1	584 ± 2	30	-29 ± 2	900 ± 200	8 ± 1	575 ± 2	1.50 ± 0.03
Mj	-66 ± 3	13 ± 2	534 ± 9	30	-59 ± 6	950 ± 450	2 ± 1	568 ± 10	1.91 ± 0.08

Electrochemical Simulations Suggest Slight Catalytic Variation Across the NiRd Series

In the native [NiFe] hydrogenase enzyme, the key Ni-L intermediate features a $Ni^{I}Fe^{II}$ center with a terminally coordinating, protonated thiolate residue,[3,41] preceding formation of the Ni-C state with a formal Ni^{III}-μH-Fe^{II} state. Quantitative electrochemical simulations have suggested an analogous CECEC mechanism for hydrogen evolution (**Figure 3A**) by electrostatically adsorbed

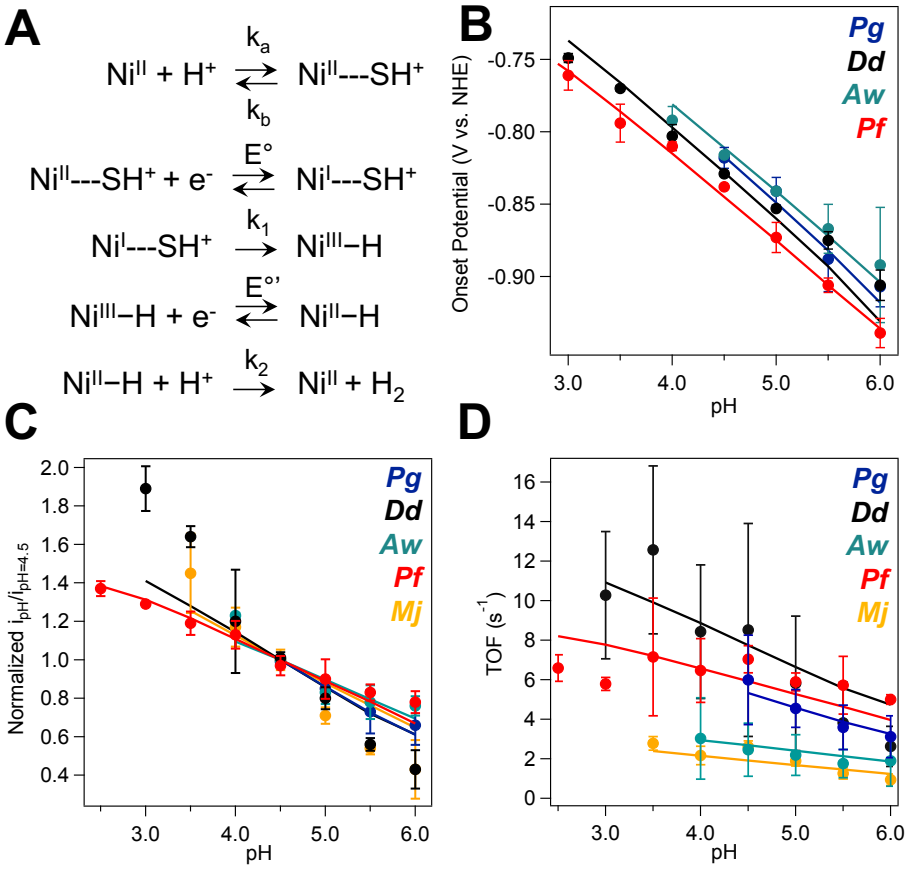

Figure 3. (**A**) Proposed mechanism for hydrogen generation by NiRd. This CECEC mechanism was used for electrochemical simulations of the *Pg* (blue), *Dd* (black), *Aw* (teal), *Pf* (red), and *Mj* (yellow) Rd variants. (**B**) - (**C**) pH-dependence of simulated (B) onset potentials and (C) normalized currents (solid lines) overlaid with experimental results (markers). The current at each pH value (i_{pH}) was divided by the average of the current measured before and after the pH of interest from CVs run at pH 4.5 ($i_{pH}/ i_{pH\ 4.5}$) (Figure S17). The *Mj* variant is not shown in (**B**) because catalysis was limited above pH 4.5, making it difficult to obtain an accurate onset potential. (**D**) Simulated TOFs overlaid on experimental results. A description of how the model parameters were selected is given in Appendix 1.

Dd NiRd on the basis of (i) a pH-dependent onset potential with a slope of 59 mV/pH unit, which

suggests a proton-coupled electron transfer (PCET) process; (ii) a nearly pH-independent TOF, which suggests that intermolecular proton transfer from solution is not the rate-determining step (RDS); and (iii) a normal kinetic isotope effect of ~4, which suggests a proton-dependent RDS.[15] To probe the mechanism of electrocatalytic hydrogen evolution by the NiRd variants, pH- and isotope dependent electrochemical studies were performed on the covalently attached proteins. As with he *Dd* NiRd, all variants exhibit pH-dependent onset potentials (**Figure 3B,** Figure S18), minimal pH-dependence of catalytic currents when normalized to those measured at pH 4.5 (i_{pH}/ $i_{pH=4.5}$) (**Figure 3C**), and a normal but small KIE (Figure S8).

We note that the KIEs for each of the covalently attached variants, including *Dd*, were approximately two-fold lower than what was previously seen for the electrostatically adsorbed *Dd* variant.[15] While it is difficult to elucidate the molecular origin of this lower KIE, it may relate to the lower overall TOF for the attached variants relative to the adsorbed systems. This small KIE also confounded attempts to use a proton inventory analysis to probe the number of protons involved in the RDS (Figure S8). However, though the pH range that could be accessed differs slightly for each variant owing to changes in protein stability (Table ST2), the simplest model that reproduces the pH-dependent onset potentials and nearly pH-independent currents involves a CECEC mechanism for all variants.

Through electrochemical simulations, the pK_a values, intrinsic reduction potentials, and the elementary rate constant for the intramolecular proton transfer step, k_1, could be constrained (Table 2, Appendix 1). To determine the pK_a of the initial chemical step, which is attributed to

Table 2. Modeled catalytic parameters for each variant using the CECEC mechanism shown in Figure 3A.

Variant	k_1 (s^{-1})	E° (V)	pK_a
Pg	16	-0.67	1.5
Dd	15	-0.68	1.5
Aw	4	-0.70	2
Pf	14	-0.73	2
Mj	6	-0.85	0.5

protonation of one of the cysteine residues, the pH-dependent normalized currents were used (**Figure 3C**). The pK_a was constrained by the slope of the values, with lower pK_as resulting in a steeper modeled slope. Because the *Mj*, *Pg* and *Dd* variants have steeper experimental slopes than the others, lower pK_a values are indicated. The modeled pK_a values across the variants range from 0.5 to 2.0, suggesting a role of the local protein environment in modulating the basicity of the coordinating cysteines.[42,43] The rate of intramolecular proton transfer (k_1) was constrained by matching the simulated and experimental TOFs as a function of pH, with a higher simulated k_1 value resulting in higher TOF values. The modeled k_1 values fall in a narrow range from 4 s^{-1} to 16 s^{-1} (**Figure 3D**), lower than those used to simulate fits for electrostatically adsorbed NiRd,[15] but in line with the lower overall TOFs obtained with covalent attachment.[28] Finally, the intrinsic reduction potential of the protonated species (E°) was modeled by identifying the value in best agreement with the observed onset potentials for catalysis; varying this value shifted the onset potential but retained the lineshape across the pH range studied. The effects of varying each parameter on the modeled values are detailed in Appendix I.

Temperature-Dependent Variation in Activity Correlates with Environment of Parent Organism

Variable temperature electrochemical experiments were performed to determine the effects of temperature on NiRd variant activity. All variants were stable across the studied temperature range (4˚C – 37˚C; Figure S19). At 4°C, the Rd from the psychrophilic organism was the most active, and the Rds from the (hyper)thermophiles were the least active. The opposite trend was seen at the highest temperatures studied, where the Rds from the hyperthermophiles were the most active. Using an Eyring analysis, a systematic trend was observed between the enthalpies of activation, which increase with organism growth temperature, and entropies of activation, which decrease in magnitude with organism growth temperature (**Figure 4**, Table ST3).[44] The activation enthalpy increase and activation entropy decrease occur with similar energetic magnitude, suggestive of entropy-enthalpy compensation. As previously noted for both electrostatically adsorbed and covalently attached *Dd* NiRd, the entropy of activation is negative across each of the variants, indicating an ordered transition state and consistent with a rate-determining, intramolecular proton transfer process.

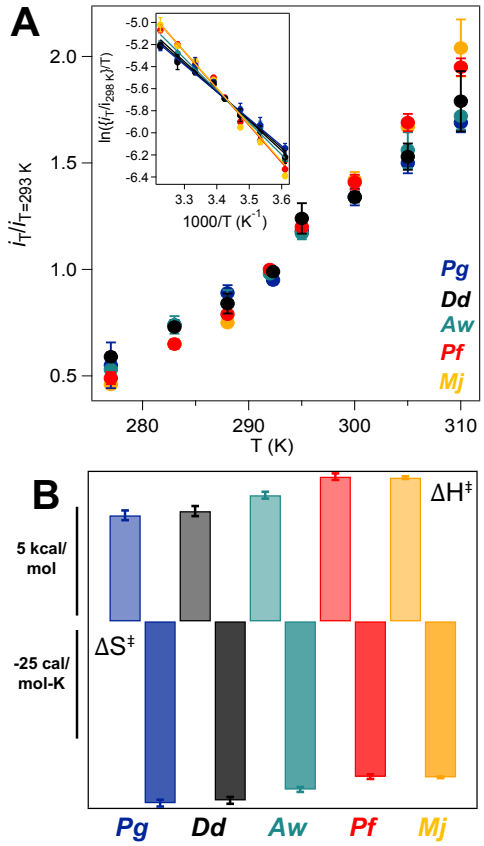

Figure 4. (A) Normalized catalytic currents as a function of temperature for each NiRd variant. All values were normalized to the current values at room temperature (Figure S9). (*Inset*) Eyring plot of each NiRd variant shown with a linear fit. (B) Enthalpies and entropies of activation for each NiRd variant based on the Eyring analysis in panel (A). Numerical values are given in Table ST3.

To complement the electrochemical studies, gas chromatography (GC) quantification of H_2 was used to assess solution-phase activity of the variants (**Figure 5**).[45,46]

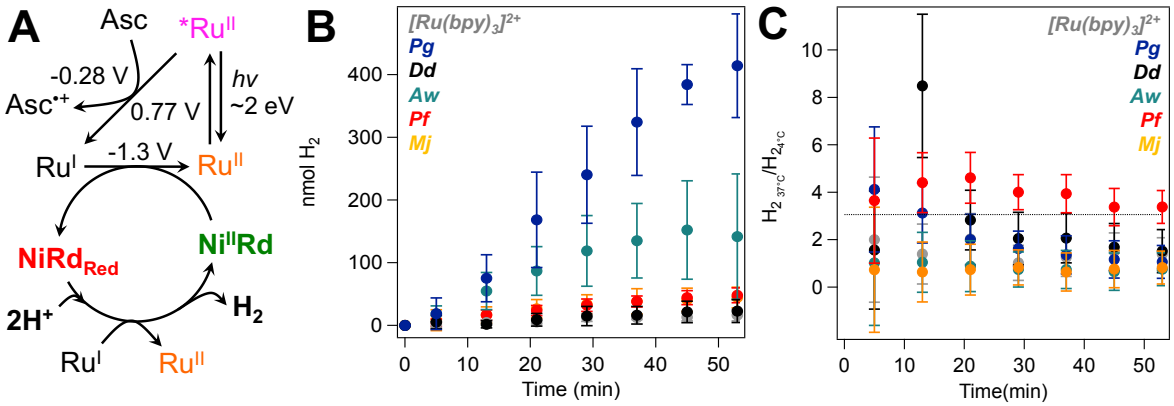

Figure 5. Light-driven hydrogen evolution assays (**A**) Schematic representation of the process for light-driven activation of NiRd. (**B**) GC quantification of H_2 produced in light-driven solution-phase assays containing 10 µm $[Ru(bpy)_3]^{2+}$ and 10 µM NiRd variant, with the control (*grey*) lacking any NiRd. Assays were performed at 4°C in 1 M phosphate buffer, pH 6.5, with 100 mM ascorbate. Assays were measured for one hour to reach a plateau of H_2 evolution activity. (**C**) Relative ratios of solution-phase H_2 production at 37°C to 4°C for each NiRd variant and the $[Ru(bpy)_3]^{2+}$ control as measured by gas chromatography analysis. The exponential Arrhenius factor (3.06) is shown as a dotted line.

It should be noted that photochemical assays can be difficult to interpret as there can be additional interactions between the photosensitizer, sacrificial electron donor, and catalyst. However, these experiments provide direct support for light-driven H_2 evolution, while bulk electrolysis of metalloproteins can result in degradation.[13] With this in mind, it was seen that all NiRd variants are active for hydrogen generation, with the amount of H_2 produced dependent on the variant. Specifically, the *Pg* and *Aw* NiRds were highly active, while the *Dd* variant was the least active, producing only slightly more H_2 than the control sample (**Figure 5B**, Figure S20). Variable temperature GC assays also indicated differential activity across the variants (**Figure 5C**). The activity of the *Pf*, *Pg,* and *Dd* variants increased at 37°C relative to 4°C, as expected from standard Arrhenius behavior, while the activities of the *Mj* and *Aw* variants were unaffected by the higher temperature. Though the *Pg* NiRd was the most active variant at all temperatures measured, the relative increase in activity was greater for the NiRd from the hyperthermophilic *Pf*, which shows

an approximately 3.9-fold increase at 37 minutes at 37 ˚C relative to the 1.4-fold increase seen for *Pg* NiRd (**Figure 5C**). As all variants are stable up to 40 ºC (Figure S19), the differences in activity cannot be simply explained by a loss of protein stability.

Paramagnetic NMR Spectroscopy Offers Insight into Dynamical Effects

Experimental measures of protein dynamics have included the use of variable temperature fluorescence studies, which reveal transient access to quenching molecules, and kinetic isotope effect studies, which can reveal the presence of a promoting, proton-dependent vibration.[47,48] However, neither set of experiments were informative for probing Rd dynamics (Figure S21). The kinetic isotope effect was observed to be temperature-independent for the *Pf*, *Dd*, and *Pg* variants, suggesting this is not the origin of the increased solution-phase activity in the *Pg* variant (Table ST4). To better understand the molecular origin underpinning the activity differences across the Rd variants, paramagnetic NMR studies were employed. ^{1}H NMR spectra of the NiRd and ZnRd variants were collected on 80 MHz, 400 MHz, and 850 MHz spectrometers at room temperature (298 K). Limitations in the spectrometer bandwidth causes uneven excitation profiles across a large sweep width at higher fields, rendering the 80 MHz spectrometer optimal for studying the extremely down-shifted peaks observed for NiRd (Figure S22). The 400 MHz and 850 MHz spectrometers are suitable for studying the central protein region, though limitations in the excitation profile can still be observed above 10 ppm and below -2 ppm on the 850 MHz spectrometer (Figure S25). To minimize these artifacts, spectra from the 400 MHz instrument were used for analysis.

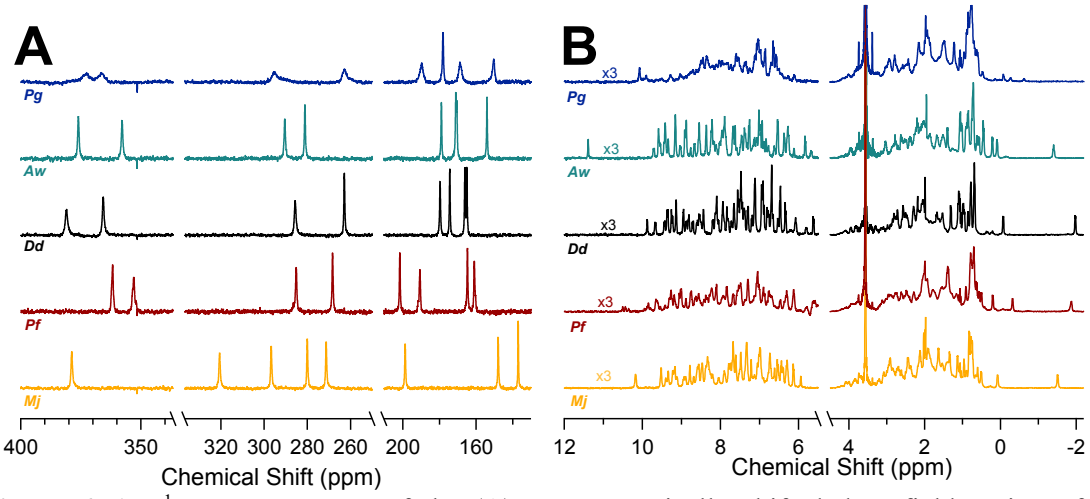

Figure 6. 1D ^{1}H NMR spectra of the (**A**) paramagnetically shifted downfield region of nickel-substituted and (**B**) protein region of zinc-substituted rubredoxin from *Pg* (blue), *Aw* (teal), *Dd* (black), *Pf* (red), and *Mj* (yellow). The spectra in (**A**) and (**B**) were collected on 80 MHz and 400 MHz spectrometers, respectively.

The downfield region of all NiRd variants (**Figure 6A**) shows 8 well-resolved signals with similar peak patterns, including four signals between 100 – 200 ppm, two signals between 250 – 300 ppm, and two signals between 350 – 400 ppm. Distinct differences observed among the selected variants are (1) the peak positions of *Mj* NiRd and (2) substantially broader linewidths in *Pg* NiRd. With respect to the first point, despite shifted downfield peaks of *Mj* NiRd, the protein region of all variants shows no distinct difference in peak positions for both NiRd and ZnRd, suggesting the fold is maintained. However, significant linewidth broadening is still observed in the protein region for both *Pg* NiRd (Figure S26) and *Pg* ZnRd (**Figure 6B**). To better understand the relationship between linewidth broadening and the source organism for the rubredoxin variants, variable temperature NMR experiments were conducted at 4 °C, 25 °C, and 37 °C (Figures S27-31). Overall, the peak linewidths of most variants narrow slightly with increasing temperature, while the *Pg* shows a dramatic change across the temperature range studied (Table ST5, Figure S32).

DISCUSSION

Variations in Primary Protein Sequence Are Not Fully Predictive of Differences in Activity

Only small differences were observed between the variants for electrochemical H_2 evolution, indicating that changes in the primary Rd sequence are not sufficient predictors of NiRd activity. However, because all variants are catalytically active, it is possible to study how subtle changes in sequence may influence the elementary parameters associated with catalysis. One notable example of this is found in the pK_a governing the first proton transfer step, which has been attributed to protonation of one of the nickel thiolate ligands. Simulations of the onset potentials and catalytic currents as a function of pH of the *Pf* Rd variant require a slight increase in pK_a in order to reproduce the experimental results. The *Pf* Rd variant also shows the best agreement with the model overall using a simple CECEC mechanism, while deviations from the modeled values are seen across the other systems (**Figure 3C**). Our inability to better reproduce the electrocatalytic behavior of the other variants, such as the *Dd* and *Mj* variant, across all measurable parameters may indicate that they use parallel reaction mechanisms or access multiple conformational states throughout the catalytic cycle, such that the currents cannot be simulated with a simple CECEC mechanism. Further analysis is beyond the scope of this work; however, it is clear from the differential pH-dependence that the pK_a values differ measurably across the variants (Appendix 1). Efforts are ongoing to directly probe protonation of the NiRd cysteine thiolate using spectroscopic techniques.

Trends in Enthalpy and Entropy of Activation of Artificial Metalloenzymes Mirror Naturally Occurring Enzymes

Variable temperature electrochemical data demonstrate that the enthalpy of activation ($\Delta H^{\ddagger}$) is lowest for *Pg* NiRd, the psychrophile-derived artificial enzyme, and increases as the growth temperature of the parent organism increases. The lower values of $\Delta H^{\ddagger}$ correlate with reduced thermal variation in activity, which is manifested as a shallower dependence of the catalytic currents on temperature for the psychrophilic *Pg* NiRd (**Figure 4**). Lower values of $\Delta H^{\ddagger}$ are also seen in naturally occurring psychrophilic enzymes relative to mesophilic or hyperthermophilic homologs.[49,50] This is attributed to reliance on a more flexible framework and fewer enthalpy-driven interactions during substrate activation,[51] allowing psychrophilic enzymes to maintain adequate catalytic rates at low temperatures.

On the other hand, the entropy of activation ($\Delta S^{\ddagger}$) is larger and more negative for *Pg* NiRd compared to the other variants. A large, negative $\Delta S^{\ddagger}$ is also seen in native enzymes from psychrophiles and is attributed to a large increase in order between the relatively relaxed ground state, with a high number of accessible microstates, and an organized transition state.[52] The broader distribution of conformational states in the ground state is attributed to catalytic site flexibility.[52,53] A smaller, less negative $\Delta S^{\ddagger}$ is likewise seen for the Rds from the hyperthermophiles, *Mj* and *Pf*. Though NiRd has not naturally evolved to produce hydrogen gas, we consider it to be interesting that similar correlations between the parent organism growth temperature and $\Delta H^{\ddagger}$ and $\Delta S^{\ddagger}$ are observed across both engineered and naturally occurring enzymes. However, native hyperthermophilic enzymes, including hydrogenases, have been shown to have even higher rates of increased activity as the temperature is raised than what is seen with the Rd platform.[54]

Much work has been conducted to study sequence-based structural and dynamical differences that influence kinetic parameters and thermodynamic stability in naturally occurring enzymes. A variety of factors may contribute to the decreased thermostability of proteins from psychrophilic

organisms, including fewer stabilizing residues such as isoleucine, which contribute to the hydrophobic effect, and lysine and glutamate residues, which have been suggested to increase thermostability through salt bridges and hydrogen bonding interactions.[55–57] While variations differ across each protein, the decrease in thermostability is tightly linked to the need for psychrophiles to maintain enzymatic rates sufficient for cellular function at low temperatures, which generally results in a more flexible protein framework.[52] Work by Herschlag and coworkers mapped temperature-associated residues in hundreds of bacterial enzyme families and identified residues associated with both high and low growth temperatures.[55] However, the sequences of the Rd variants selected in this work do not follow the residue trends seen across the large sample of bacterial enzyme families (Figure S33), highlighting that amino acid sequence is not (yet) sufficient to predict activity in this artificial enzyme.

Dynamical Effects May Influence Activity in the *Pg* Variant

TOF values of *Pg* NiRd are independent of whether the protein is adsorbed or attached. We postulate that this retention of activity may derive from the dynamics of a more flexible protein, which can more easily access low-energy conformational changes. This would support the hypothesis that the decreased TOFs for covalently anchored NiRd are caused by reduced protein motion. In native psychrophilic organisms, a more flexible backbone has been attributed to higher catalytic activity.[52] We note that *Pg* NiRd is more active for solution phase hydrogen production than the previously studied *Dd* NiRd sequence. This same activity may not be seen on an electrode surface, as mobility may be specifically or nonspecifically constrained upon adsorption or attachment to an electrode, giving rise to the low electrochemical TOFs observed.

To gain experimental support for the role of increased dynamics in the activity of the *Pg* NiRd, paramagnetic NMR studies were employed. The paramagnetic ^{1}H NMR spectrum of nickel-substituted rubredoxin (from *Desulfovibrio vulgaris)* was first reported by Goodfellow and coworkers in 2009.[58] The eight well-resolved, non-exchangeable proton peaks observed in the downfield spectral region (400 – 100 ppm) were assigned to the active-site cysteine β-CH_2 protons, with the dramatic shifts resulting from Fermi contact contributions from the metal center. Taking into account that all rubredoxins have the same tetra-cysteinate coordination to the metal with a distorted tetrahedral geometry, the corresponding assignment was made for the downfield peaks in the NiRd variants studied here (**Figure 6A**). That similar peak positions are observed across most of the variants suggests a similar spatial orientation. Hence, the drastic difference in peak position and patterns observed for *Mj* NiRd can likely be attributed to a different spatial arrangement of the cysteine β-CH_2 protons in the non-canonical CXC metal binding loop.

Linewidth broadening observed in both downfield and protein regions of *Pg* NiRd was hypothesized to derive from motions on the μs – ms timescale.[59] Both structural heterogeneity[60] and conformational exchange can contribute to broadened linewidths. The latter may derive from higher structural flexibility, which is proposed to be one of the key properties of enzymes from psychrophilic organisms.[53,61,62] Because similar lineshapes are observed in the diamagnetic analogue, *Pg* ZnRd, a dominant contribution from the paramagnetic metal center can be ruled out. The differences in linewidth between the mesophile- and hyperthermophile-derived variants are more subtle.

Variable temperature experiments showed an increase in linewidth with decreasing temperature in all variants.[63] While a quantitative linewidth analysis cannot yet be performed, as it would require global ^{13}C and ^{15}N labeling and multidimensional NMR experiments, these analyses represent

future objectives in this project. However, semi-quantitative analyses performed on isolated signals can provide insight into changes across variants. The most up-field shifted signals in the ZnRd variants, proposed to be from side-chain methyl groups, were selected for full-width half-maximum (FWHM) linewidth analysis (Table ST5). While the same trends are observed in all variants, the *Pg* ZnRd showed the largest deviation across the temperature range (Figure S32), and the linewidth is substantially larger, especially at low temperatures. This observation is indicative of a relationship between structural flexibility, activity, and biological origin of the protein scaffold. These initial findings set the framework for more extensive studies to explore the molecular contributors to local and global flexibility among other Rd variants and correlate these motions with catalysis.

CONCLUSIONS

This study establishes the broad applicability of nickel-substituted rubredoxin homologs as functional [NiFe] hydrogenase model enzymes and suggests that considering the environmental origin of the sequence of the protein scaffold can be important. Differential relative activity between electrochemical and solution-phase activity in the *Pg* variant suggests that the flexibility of this psychrophilic protein may play a role in catalysis. The distinctly broad NMR spectral linewidths support this hypothesis. The behavior of the diverse Rds studied here suggests that activity of the artificial enzyme can be correlated to the growth temperature of the parent organism, with similar trends observed between artificial and naturally occurring enzymes. As this work characterizes an admittedly small, hand-picked sample set, future work will focus on developing a screening method for expanding the library and using advanced spectroscopic methods to further resolve the molecular-level contributors underpinning these results.

ASSOCIATED CONTENT

Supporting Information.

The following files are available free of charge. Supplemental figures, tables, sample scripts, and details on electrochemical simulations (PDF).

AUTHOR INFORMATION

Corresponding Author

*E-mail shafaat.1@osu.edu.

Author Contributions

The manuscript was written through contributions of all authors. All authors have given approval to the final version of the manuscript.

Funding Sources

This work was supported by the U.S. National Science Foundation (CHE-1454289) and (CHE-2108684).

Notes

The authors declare no competing financial interest.

ACKNOWLEDGMENTS

We would like to thank the National Science Foundation (CHE-1454289 and CHE-2108684) for supporting this work as well as the OSU Department of Chemistry and Biochemistry. We would also like to thank members of the Shafaat laboratory, especially Regina Treviño, for their feedback

and advice. We thank Francis E. Jenney (Philadelphia College of Osteopathic Medicine- Georgia) for his generous donation of the *Pf* Rd plasmid.

REFERENCES

(1) van Renssen, S. The Hydrogen Solution? *Nature Climate Change* **2020**, *10* (9), 799–801. https://doi.org/10.1038/s41558-020-0891-0.
(2) Turner, J. A. Sustainable Hydrogen Production. *Science* **2004**, *305* (5686), 972–974. https://doi.org/10.1126/science.1103197.
(3) Lubitz, W.; Ogata, H.; Rüdiger, O.; Reijerse, E. Hydrogenases. *Chem. Rev.* **2014**, *114* (8), 4081–4148. https://doi.org/10.1021/cr4005814.
(4) Vignais, P. M.; Billoud, B. Occurrence, Classification, and Biological Function of Hydrogenases: An Overview. *Chem. Rev.* **2007**, *107* (10), 4206–4272. https://doi.org/10.1021/cr050196r.
(5) Foerster, S.; Stein, M.; Brecht, M.; Ogata, H.; Higuchi, Y.; Lubitz, W. Single Crystal EPR Studies of the Reduced Active Site of [NiFe] Hydrogenase from *Desulfovibrio Vulgaris* Miyazaki F. *J. Am. Chem. Soc.* **2003**, *125* (1), 83–93. https://doi.org/10.1021/ja027522u.
(6) Shafaat, H. S. 8.27 - [NiFe] Hydrogenases: A Paradigm for Bioinorganic Hydrogen Conversion. In *Comprehensive Coordination Chemistry III*; Constable, E. C., Parkin, G., Que Jr, L., Eds.; Elsevier: Oxford, 2021; pp 707–730. https://doi.org/10.1016/B978-0-08-102688-5.00056-8.
(7) De Lacey, A. L.; Fernández, V. M.; Rousset, M.; Cammack, R. Activation and Inactivation of Hydrogenase Function and the Catalytic Cycle: Spectroelectrochemical Studies. *Chem. Rev.* **2007**, *107* (10), 4304–4330. https://doi.org/10.1021/cr0501947.
(8) Pandelia, M.-E.; Lubitz, W.; Nitschke, W. Evolution and Diversification of Group 1 [NiFe] Hydrogenases. Is There a Phylogenetic Marker for O2-Tolerance? *Biochimica et Biophysica Acta (BBA) - Bioenergetics* **2012**, *1817* (9), 1565–1575. https://doi.org/10.1016/j.bbabio.2012.04.012.
(9) Lambertz, C.; Leidel, N.; Havelius, K. G. V.; Noth, J.; Chernev, P.; Winkler, M.; Happe, T.; Haumann, M. O2 Reactions at the Six-Iron Active Site (H-Cluster) in [FeFe]-Hydrogenase*. *Journal of Biological Chemistry* **2011**, *286* (47), 40614–40623. https://doi.org/10.1074/jbc.M111.283648.
(10) Saint-Martin, P.; Lespinat, P. A.; Fauque, G.; Berlier, Y.; LeGall, J.; Moura, I.; Teixeira, M.; Xavier, A. V.; Moura, J. J. G. Hydrogen Production and Deuterium-Proton Exchange Reactions Catalyzed by Desulfovibrio Nickel(II)-Substituted Rubredoxins. *Proceedings of the National Academy of Sciences* **1988**, *85* (24), 9378–9380. https://doi.org/10.1073/pnas.85.24.9378.
(11) May, S. W.; Kuo, J.-Y. Preparation and Properties of Cobalt(II) Rubredoxin. *Biochemistry* **1978**, *17* (16), 3333–3338.
(12) Huang, Y. H.; Moura, I.; Moura, J. J. G.; LeGall, J.; Park, J. B.; Adams, M. W. W.; Johnson, M. K. Resonance Raman Studies of Nickel Tetrathiolates and Nickel-Substituted Rubredoxins and Desulforedoxin. *Inorg. Chem.* **1993**, *32* (4), 406–412. https://doi.org/10.1021/ic00056a012.

(13) Slater, J. W.; Shafaat, H. S. Nickel-Substituted Rubredoxin as a Minimal Enzyme Model for Hydrogenase. *J. Phys. Chem. Lett.* **2015**, *6* (18), 3731–3736. https://doi.org/10.1021/acs.jpclett.5b01750.
(14) Jenney, F. E.; Adams, M. W. W. [5] Rubredoxin from Pyrococcus Furiosus. In *Methods in Enzymology*; Elsevier, 2001; Vol. 334, pp 45–55. https://doi.org/10.1016/S0076-6879(01)34457-9.
(15) Slater, J. W.; Marguet, S. C.; Monaco, H. A.; Shafaat, H. S. Going beyond Structure: Nickel-Substituted Rubredoxin as a Mechanistic Model for the [NiFe] Hydrogenases. *J. Am. Chem. Soc.* **2018**, *140* (32), 10250–10262. https://doi.org/10.1021/jacs.8b05194.
(16) Slater, J. W.; Marguet, S. C.; Gray, M. E.; Monaco, H. A.; Sotomayor, M.; Shafaat, H. S. Power of the Secondary Sphere: Modulating Hydrogenase Activity in Nickel-Substituted Rubredoxin. *ACS Catal.* **2019**, *9* (10), 8928–8942. https://doi.org/10.1021/acscatal.9b01720.
(17) Shafaat, H. S.; Rüdiger, O.; Ogata, H.; Lubitz, W. [NiFe] Hydrogenases: A Common Active Site for Hydrogen Metabolism under Diverse Conditions. *Biochimica et Biophysica Acta (BBA) - Bioenergetics* **2013**, *1827* (8–9), 986–1002. https://doi.org/10.1016/j.bbabio.2013.01.015.
(18) Peters, J. W.; Schut, G. J.; Boyd, E. S.; Mulder, D. W.; Shepard, E. M.; Broderick, J. B.; King, P. W.; Adams, M. W. W. [FeFe]- and [NiFe]-Hydrogenase Diversity, Mechanism, and Maturation. *Biochimica et Biophysica Acta (BBA) - Molecular Cell Research* **2015**, *1853* (6), 1350–1369. https://doi.org/10.1016/j.bbamcr.2014.11.021.
(19) Blake, P. R.; Park, J. B.; Bryant, F. O.; Aono, S.; Magnuson, J. K.; Eccleston, E.; Howard, J. B.; Summers, M. F.; Adams, M. W. W. Determinants of Protein Hyperthermostability: Purification and Amino Acid Sequence of Rubredoxin from the Hyperthermophilic Archaebacterium Pyrococcus Furiosus and Secondary Structure of the Zinc Adduct by NMR. *Biochemistry* **1991**, *30* (45), 10885–10895. https://doi.org/10.1021/bi00109a012.
(20) *CDD Conserved Protein Domain Family: rubredoxin*. https://www-ncbi-nlm-nih-gov.proxy.lib.ohio-state.edu/Structure/cdd/cd00730 (accessed 2023-04-25).
(21) Zallot, R.; Oberg, N.; Gerlt, J. A. The EFI Web Resource for Genomic Enzymology Tools: Leveraging Protein, Genome, and Metagenome Databases to Discover Novel Enzymes and Metabolic Pathways. *Biochemistry* **2019**, *58* (41), 4169–4182. https://doi.org/10.1021/acs.biochem.9b00735.
(22) Shannon, P.; Markiel, A.; Ozier, O.; Baliga, N. S.; Wang, J. T.; Ramage, D.; Amin, N.; Schwikowski, B.; Ideker, T. Cytoscape: A Software Environment for Integrated Models of Biomolecular Interaction Networks. *Genome Res.* **2003**, *13* (11), 2498–2504. https://doi.org/10.1101/gr.1239303.
(23) Robert, X.; Gouet, P. Deciphering Key Features in Protein Structures with the New ENDscript Server. *Nucleic Acids Research* **2014**, *42* (W1), W320–W324. https://doi.org/10.1093/nar/gku316.
(24) Madeira, F.; Pearce, M.; Tivey, A. R. N.; Basutkar, P.; Lee, J.; Edbali, O.; Madhusoodanan, N.; Kolesnikov, A.; Lopez, R. Search and Sequence Analysis Tools Services from EMBL-EBI in 2022. *Nucleic Acids Research* **2022**, *50* (W1), W276–W279. https://doi.org/10.1093/nar/gkac240.
(25) Crooks, G. E.; Hon, G.; Chandonia, J.-M.; Brenner, S. E. WebLogo: A Sequence Logo Generator. *Genome Res* **2004**, *14* (6), 1188–1190. https://doi.org/10.1101/gr.849004.

(26) Jumper, J.; Evans, R.; Pritzel, A.; Green, T.; Figurnov, M.; Ronneberger, O.; Tunyasuvunakool, K.; Bates, R.; Žídek, A.; Potapenko, A.; Bridgland, A.; Meyer, C.; Kohl, S. A. A.; Ballard, A. J.; Cowie, A.; Romera-Paredes, B.; Nikolov, S.; Jain, R.; Adler, J.; Back, T.; Petersen, S.; Reiman, D.; Clancy, E.; Zielinski, M.; Steinegger, M.; Pacholska, M.; Berghammer, T.; Bodenstein, S.; Silver, D.; Vinyals, O.; Senior, A. W.; Kavukcuoglu, K.; Kohli, P.; Hassabis, D. Highly Accurate Protein Structure Prediction with AlphaFold. *Nature* **2021**, *596* (7873), 583–589. https://doi.org/10.1038/s41586-021-03819-2.

(27) Varadi, M.; Anyango, S.; Deshpande, M.; Nair, S.; Natassia, C.; Yordanova, G.; Yuan, D.; Stroe, O.; Wood, G.; Laydon, A.; Žídek, A.; Green, T.; Tunyasuvunakool, K.; Petersen, S.; Jumper, J.; Clancy, E.; Green, R.; Vora, A.; Lutfi, M.; Figurnov, M.; Cowie, A.; Hobbs, N.; Kohli, P.; Kleywegt, G.; Birney, E.; Hassabis, D.; Velankar, S. AlphaFold Protein Structure Database: Massively Expanding the Structural Coverage of Protein-Sequence Space with High-Accuracy Models. *Nucleic Acids Research* **2022**, *50* (D1), D439–D444. https://doi.org/10.1093/nar/gkab1061.

(28) Treviño, R. E.; Slater, J. W.; Shafaat, H. S. Robust Carbon-Based Electrodes for Hydrogen Evolution through Site-Selective Covalent Attachment of an Artificial Metalloenzyme. *ACS Appl. Energy Mater.* **2020**, *3* (11), 11099-11112. acsaem.0c02069. https://doi.org/10.1021/acsaem.0c02069.

(29) Laviron, E. General Expression of the Linear Potential Sweep Voltammogram in the Case of Diffusionless Electrochemical Systems. *Journal of Electroanalytical Chemistry and Interfacial Electrochemistry* **1979**, *101* (1), 19–28. https://doi.org/10.1016/S0022-0728(79)80075-3.

(30) Fourmond, V.; Hoke, K.; Heering, H. A.; Baffert, C.; Leroux, F.; Bertrand, P.; Léger, C. SOAS: A Free Program to Analyze Electrochemical Data and Other One-Dimensional Signals. *Bioelectrochemistry* **2009**, *76* (1–2), 141–147. https://doi.org/10.1016/j.bioelechem.2009.02.010.

(31) Bard, A. J.; Faulkner, L. R. *Electrochemical Methods: Fundamentals and Applications*, 2nd ed.; Wiley: New York, 2001.

(32) Jeuken, L. J. C.; McEvoy, J. P.; Armstrong, F. A. Insights into Gated Electron-Transfer Kinetics at the Electrode−Protein Interface: A Square Wave Voltammetry Study of the Blue Copper Protein Azurin. *J. Phys. Chem. B* **2002**, *106* (9), 2304–2313. https://doi.org/10.1021/jp0134291.

(33) Bau, R.; Rees, D. C.; Kurtz Jr., D. M.; Scott, R. A.; Huang, H.; Adams, M. W. W.; Eidsness, M. K. Crystal Structure of Rubredoxin from Pyrococcus Furiosus at 0.95 Å Resolution, and the Structures of N-Terminal Methionine and Formylmethionine Variants of Pf Rd. Contributions of N-Terminal Interactions to Thermostability. *JBIC* **1998**, *3* (5), 484–493. https://doi.org/10.1007/s007750050258.

(34) Moghadam, M. S.; Albersmeier, A.; Winkler, A.; Cimmino, L.; Rise, K.; Hohmann-Marriott, M. F.; Kalinowski, J.; Rückert, C.; Wentzel, A.; Lale, R. Isolation and Genome Sequencing of Four Arctic Marine Psychrobacter Strains Exhibiting Multicopper Oxidase Activity. *BMC Genomics* **2016**, *17* (1), 117. https://doi.org/10.1186/s12864-016-2445-4.

(35) Day, M. W.; Hsu, B. T.; Joshua-Tor, L.; Park, J. B.; Zhou, Z. H.; Adams, M. W.; Rees, D. C. X-Ray Crystal Structures of the Oxidized and Reduced Forms of the Rubredoxin from the Marine Hyperthermophilic Archaebacterium Pyrococcus Furiosus. *Protein Sci* **1992**, *1* (11), 1494–1507. https://doi.org/10.1002/pro.5560011111.

(36) Slater, J. W.; Marguet, S. C.; Cirino, S. L.; Maugeri, P. T.; Shafaat, H. S. Experimental and DFT Investigations Reveal the Influence of the Outer Coordination Sphere on the Vibrational Spectra of Nickel-Substituted Rubredoxin, a Model Hydrogenase Enzyme. *Inorg. Chem.* **2017**, *56* (7), 3926–3938. https://doi.org/10.1021/acs.inorgchem.6b02934.
(37) Sheridan, M. V.; Lam, K.; Geiger, W. E. An Anodic Method for Covalent Attachment of Molecules to Electrodes through an Ethynyl Linkage. *J. Am. Chem. Soc.* **2013**, *135* (8), 2939–2942. https://doi.org/10.1021/ja312405h.
(38) Chidsey, C. E. D. Free Energy and Temperature Dependence of Electron Transfer at the Metal-Electrolyte Interface. *Science* **1991**, *251* (4996), 919–922. https://doi.org/10.1126/science.251.4996.919.
(39) Mann, J. A.; Rodríguez-López, J.; Abruña, H. D.; Dichtel, W. R. Multivalent Binding Motifs for the Noncovalent Functionalization of Graphene. *J. Am. Chem. Soc.* **2011**, *133* (44), 17614–17617. https://doi.org/10.1021/ja208239v.
(40) Zitare, U. A.; Szuster, J.; Scocozza, M. F.; Espinoza-Cara, A.; Leguto, A. J.; Morgada, M. N.; Vila, A. J.; Murgida, D. H. The Role of Molecular Crowding in Long-Range Metalloprotein Electron Transfer: Dissection into Site- and Scaffold-Specific Contributions. *Electrochimica Acta* **2019**, *294*, 117–125. https://doi.org/10.1016/j.electacta.2018.10.069.
(41) Hidalgo, R.; Ash, P. A.; Healy, A. J.; Vincent, K. A. Infrared Spectroscopy During Electrocatalytic Turnover Reveals the Ni-L Active Site State During H2 Oxidation by a NiFe Hydrogenase. *Angewandte Chemie International Edition* **2015**, *54* (24), 7110–7113. https://doi.org/10.1002/anie.201502338.
(42) Lim, J. C.; Gruschus, J. M.; Kim, G.; Berlett, B. S.; Tjandra, N.; Levine, R. L. A Low PKa Cysteine at the Active Site of Mouse Methionine Sulfoxide Reductase A. *J Biol Chem* **2012**, *287* (30), 25596–25601. https://doi.org/10.1074/jbc.M112.369116.
(43) Zhang, Z. Y.; Dixon, J. E. Active Site Labeling of the Yersinia Protein Tyrosine Phosphatase: The Determination of the PKa of the Active Site Cysteine and the Function of the Conserved Histidine 402. *Biochemistry* **1993**, *32* (36), 9340–9345. https://doi.org/10.1021/bi00087a012.
(44) Eyring, H. The Activated Complex in Chemical Reactions. *The Journal of Chemical Physics* **1935**, *3* (2), 107–115. https://doi.org/10.1063/1.1749604.
(45) Edwards, E. H.; Jelušić, J.; Chakraborty, S.; Bren, K. L. Photochemical Hydrogen Evolution from Cobalt Microperoxidase-11. *Journal of Inorganic Biochemistry* **2021**, *217*, 111384. https://doi.org/10.1016/j.jinorgbio.2021.111384.
(46) Deponti, E.; Natali, M. Photocatalytic Hydrogen Evolution with Ruthenium Polypyridine Sensitizers: Unveiling the Key Factors to Improve Efficiencies. *Dalton Trans.* **2016**, *45* (22), 9136–9147. https://doi.org/10.1039/C6DT01221C.
(47) Andrews, B. A.; Dyer, R. B. Comparison of the Role of Protein Dynamics in Catalysis by Dihydrofolate Reductase from E. Coli and H. Sapiens. *J. Phys. Chem. B* **2022**, *126* (37), 7126–7134. https://doi.org/10.1021/acs.jpcb.2c05112.
(48) Kohen, A.; Klinman, J. P. Protein Flexibility Correlates with Degree of Hydrogen Tunneling in Thermophilic and Mesophilic Alcohol Dehydrogenases. *J. Am. Chem. Soc.* **2000**, *122* (43), 10738–10739. https://doi.org/10.1021/ja002229k.
(49) Low, P. S.; Bada, J. L.; Somero, G. N. Temperature Adaptation of Enzymes: Roles of the Free Energy, the Enthalpy, and the Entropy of Activation. *Proc Natl Acad Sci U S A* **1973**, *70* (2), 430–432.

(50) Lonhienne, T.; Gerday, C.; Feller, G. Psychrophilic Enzymes: Revisiting the Thermodynamic Parameters of Activation May Explain Local Flexibility. *Biochim Biophys Acta* **2000**, *1543* (1), 1–10. https://doi.org/10.1016/s0167-4838(00)00210-7.
(51) Feller, G.; Gerday, C. Psychrophilic Enzymes: Hot Topics in Cold Adaptation. *Nat Rev Microbiol* **2003**, *1* (3), 200–208. https://doi.org/10.1038/nrmicro773.
(52) Goyal, D.; Swaroop, S.; Prakash, O.; Pandey, J. Survival Strategies in Cold-Adapted Microorganisms. In *Survival Strategies in Cold-adapted Microorganisms*; Goel, R., Soni, R., Suyal, D. C., Khan, M., Eds.; Springer: Singapore, 2022; pp 173–186. https://doi.org/10.1007/978-981-16-2625-8_8.
(53) Feller, G. Psychrophilic Enzymes: From Folding to Function and Biotechnology. *Scientifica* **2013**, *2013*, 1–28. https://doi.org/10.1155/2013/512840.
(54) Bryant, F. O.; Adams, M. W. Characterization of Hydrogenase from the Hyperthermophilic Archaebacterium, Pyrococcus Furiosus. *Journal of Biological Chemistry* **1989**, *264* (9), 5070–5079. https://doi.org/10.1016/S0021-9258(18)83701-2.
(55) Pinney, M. M.; Mokhtari, D. A.; Akiva, E.; Yabukarski, F.; Sanchez, D. M.; Liang, R.; Doukov, T.; Martinez, T. J.; Babbitt, P. C.; Herschlag, D. Parallel Molecular Mechanisms for Enzyme Temperature Adaptation. *Science* **2021**, *371* (6533), eaay2784. https://doi.org/10.1126/science.aay2784.
(56) Lam, S. Y.; Yeung, R. C. Y.; Yu, T.-H.; Sze, K.-H.; Wong, K.-B. A Rigidifying Salt-Bridge Favors the Activity of Thermophilic Enzyme at High Temperatures at the Expense of Low-Temperature Activity. *PLoS Biol* **2011**, *9* (3), e1001027. https://doi.org/10.1371/journal.pbio.1001027.
(57) Vieille, C.; Zeikus, G. J. Hyperthermophilic Enzymes: Sources, Uses, and Molecular Mechanisms for Thermostability. *Microbiol Mol Biol Rev* **2001**, *65* (1), 1–43. https://doi.org/10.1128/MMBR.65.1.1-43.2001.
(58) Goodfellow, B. J.; Duarte, I. C. N.; Macedo, A. L.; Volkman, B. F.; Nunes, S. G.; Moura, I.; Markley, J. L.; Moura, J. J. G. An NMR Structural Study of Nickel-Substituted Rubredoxin. *J Biol Inorg Chem* **2010**, *15* (3), 409–420. https://doi.org/10.1007/s00775-009-0613-6.
(59) Palmer, A. G. I. NMR Characterization of the Dynamics of Biomacromolecules. *Chem. Rev.* **2004**, *104* (8), 3623–3640. https://doi.org/10.1021/cr030413t.
(60) Xia, Z.; Nguyen, B. D.; Brunori, M.; Cutruzzolà, F.; La Mar, G. N. 1H-NMR Study of the Effect of Temperature through Reversible Unfolding on the Heme Pocket Molecular Structure and Magnetic Properties of Aplysia Limacina Cyano-Metmyoglobin. *Biophysical Journal* **2005**, *89* (6), 4149–4158. https://doi.org/10.1529/biophysj.105.062398.
(61) Papaleo, E.; Pasi, M.; Riccardi, L.; Sambi, I.; Fantucci, P.; Gioia, L. D. Protein Flexibility in Psychrophilic and Mesophilic Trypsins. Evidence of Evolutionary Conservation of Protein Dynamics in Trypsin-like Serine-Proteases. *FEBS Letters* **2008**, *582* (6), 1008–1018. https://doi.org/10.1016/j.febslet.2008.02.048.
(62) Roulling, F.; Piette, F.; Cipolla, A.; Struvay, C.; Feller, G. Psychrophilic Enzymes: Cool Responses to Chilly Problems. In *Extremophiles Handbook*; Horikoshi, K., Ed.; Springer Japan: Tokyo, 2011; pp 891–913. https://doi.org/10.1007/978-4-431-53898-1_43.
(63) Schütz, S.; Sprangers, R. Methyl TROSY Spectroscopy: A Versatile NMR Approach to Study Challenging Biological Systems. *Progress in Nuclear Magnetic Resonance Spectroscopy* **2020**, *116*, 56–84. https://doi.org/10.1016/j.pnmrs.2019.09.004.

For Table of Contents use only